Influence of helium incorporation on growth process and properties of aluminum thin films deposited by DC magnetron sputtering

Sara Ibrahim, Fatima Zahrae Lahboub, Pascal Brault, Agnès Petit, Amael Caillard, Eric Millon, Thierry Sauvage, Asunción Fernández, Anne-Lise Thomann

▶ To cite this version:

Sara Ibrahim, Fatima Zahrae Lahboub, Pascal Brault, Agnès Petit, Amael Caillard, et al.. Influence of helium incorporation on growth process and properties of aluminum thin films deposited by DC magnetron sputtering. Surface and Coatings Technology, 2021, 426, pp.127808. 10.1016/j.surfcoat.2021.127808 . hal-03384877

HAL Id: hal-03384877
https://hal.science/hal-03384877

Submitted on 19 Oct 2021

Influence of helium incorporation on growth process and properties of aluminum thin films deposited by DC magnetron sputtering

Sara Ibrahim [a, *], Fatima Zahrae Lahboub [a], Pascal Brault [a], Agnès Petit [a], Amaël Caillard [a], Eric Millon [a], Thierry Sauvage [b], Asunción Fernández [a,c] and Anne-Lise Thomann [a]

[a] GREMI, UMR7344 CNRS Université d'Orléans, 14 rue d'Issoudun, 45067 Orléans, France

[b] CEMHTI, UPR3079 CNRS, 1D avenue de la Recherche Scientifique, 45071 Orléans, France

[c] Instituto de Ciencia de Materiales de Sevilla, CSIC-Univ. Seville, Avda. Américo Vespucio 49, 41092 Seville, Spain

* sara.ibrahim@univ-orleans.fr

fatima-zahrae.lahboub@etu.univ-orleans.fr

pascal.brault@univ-orleans.fr

agnes.petit@univ-orleans.fr

amael.caillard@univ-orleans.fr

eric.millon@univ-orleans.fr

thierry.sauvage@cnrs-orleans.fr

asuncion@icmse.csis.es

anne-lise.thomann@univ-orleans.fr

Abstract

The effect of helium content on the morphology, crystallinity, and composition of aluminum films was investigated by depositing He-loaded Al films onto Si substrates via direct current (DC) magnetron sputtering in different Ar/He plasma mixtures. Three different plasma regimes were identified depending on the percentage of He in the gas phase. For a low He to total gas ratio ($\Gamma_{He} \leq 70\%$), the plasma is dominated by argon, where Ar^+ ions contribute to sputter out the target atoms. The films deposited in this regime exhibited the classical dense columnar structure and contain very low amount of He (below 2%). Then, as Γ_{He} increases, helium ions begin to be formed and more fast He neutrals reach the substrate, affecting the film growth. As He amount increased in the gas phase up to 95%, the proportion of He inserted in the films rised up to ~ 15 at.%. Moreover, bubbles/porosity were formed inside the films; those obtained in pure He plasma presented a highly porous fiberform nanostructure. All results confirmed that the modification of the film characteristics was related to the change of the deposition conditions when Ar was replaced by He and to the insertion/release mechanisms of He during the growth.

Keywords

Nanostructured aluminum films, porous thin films, direct current magnetron sputtering, helium-argon mixture plasma

1. Introduction

The study of helium (He) behavior in metals has drawn significant attention in the materials science community for several years. He is produced in charged tritium storage media and is inserted in the structural materials of fission and fusion reactors [1]. The accumulation of He in these materials could lead to the degradation of their mechanical properties [2]. Hence, the mechanism of He diffusion in the metal lattice is of great interest in nuclear technology, and it has been widely studied [3,4]. Due to its insolubility in metals, helium can diffuse on a long pathway and induce the formation of vacancy defects by a self-trapping mechanism, even at kinetic energies below the metal displacement threshold [5,6]. These He-vacancy complexes can act as trapping sites for other incoming He atoms until large bubbles are stabilized [7]. In certain conditions, when these processes take place close to the surface and are associated with metal atoms' mobility, flaking and nanofibers have been observed [6,8–10]. Thus, low-energy He plasma irradiation allowed synthesizing nanostructured and porous materials with tailored functionalities. These nanostructures modify the material properties and can be relevant for different applications [11–13]. For instance, Fan et al. reported the formation process of the fiberform nanostructured (fuzz) tungsten layer by He plasma irradiation [8]. The formation of metallic nanostructures by exposure to He plasmas has been also evidenced in other metals such as nickel, iron and aluminum [12,14].

Recently, magnetron sputtering has been employed as an efficient method to introduce ^{4}He and ^{3}He atoms and induce porosity formation into thin films [15–18]. Zheng et al. [1] and Shi et al. [2] obtained titanium films containing a high concentration of He by magnetron sputtering with He/Ar mixture. It has been shown that He incorporation may lead to the formation of nano-sized He filled bubbles or porous thin films depending on the material and the process parameters [15,16,13].

This work aims at determining the optimal deposition parameters to produce Al films with the highest open porosity/specific surface area for hydrothermal hydrogen production [19]. The other objective is to get better insight into the mechanism involved in the growth process. We investigated the microstructure and composition of Al thin films prepared by direct current (DC) magnetron sputtering in different He/Ar mixed atmospheres. For this purpose, different deposited films were investigated by scanning electron microscopy (SEM) and X-ray diffraction (XRD) techniques. Moreover, Rutherford backscattering spectrometry (RBS) and proton elastic backscattering spectrometry (PEBS) were carried out to determine the number of Al and He atoms in the films, respectively. Gas-phase characterization and simulations including mass spectrometry, SRIM software and collisional model have completed the study towards understanding the film's growing mechanism.

2. Materials and methods

2.1. Deposition experiments

Al films were deposited onto (100) oriented p-doped Si wafers by sputtering a 4-inch Al target (99.999% purity from Neyco). The substrates were pasted on a rotating substrate holder, and the distance between the substrate and the target was fixed at 12 cm. The system was kept under vacuum, reaching a base pressure of about 7 x 10^{-4} Pa. The discharge current was regulated to 1 A using a DC power supply (Pinnacle plus from Advanced Energy). Then, depending on the process parameters, the cathode voltage varied between 325 and 440 V, resulting in a power range of 325-440 W. The gas flow rates were adjusted using two Bronkhorst EL-FLOW mass flow controllers. The argon and helium flow rates (Φ_{Ar} and Φ_{He}) were varied to obtain a He percentage ($\Gamma_{He} = \Phi_{He} / (\Phi_{Ar} + \Phi_{He}) \times 100$) ranging between 0 and 100%. The total pressure in the chamber was settled to 1 Pa using a gate valve before turning on the discharge.

It is expected that the sputtering yield of metal atoms by He ions is much lower than that by Ar ones [20]. From Stopping and Range of Ions in Matter (SRIM) simulation [21], the sputtering yield of Al by 400 eV He^+ ions (0.29 atoms/ion) is determined to be twice less than that by 400 eV Ar^+ ions (0.58 atoms/ion). The deposition time (t_d) was chosen to deposit Al films of ~1 µm thickness (as determined from SEM measurements) in different He/Ar mixtures, as shown in Table 1. To estimate the reproducibility of the experiments, some films were deposited twice and characterized.

2.2. Gas phase characterization

SRIM software had been used to determine the nature and energy of particles emitted at the target under bombardment with 400 eV Ar or He ions. Starting from these data, a simple collisional model of particle slowing down along straight-line trajectories and subjected to a continuous energy loss process, has been implemented to determine the energy distribution functions (EDF) of the particle flux in pure argon or helium gas as a function of the distance from the source [22]. Moreover, the mean kinetic energy of the sputtered atoms was calculated according to a modification of the Thompson atomic model [22]. The sputtering gas temperature was fixed at 300 K with a pressure and a target-substrate distance values identical to the deposition conditions. Additional information about the model can be found elsewhere [22]. In addition, the influence of Γ_{He} on the ionization of Al, Ar and He was determined by measuring their ion energy distribution functions (IEDF) using a EQP1000 energy-resolved mass spectrometer (Hiden Analytical) between 1 and 20 eV in 0.1 eV/charge steps. The spectrometer was placed on the axis of the Al target with a distance of 8 cm from the electrically grounded 200 µm in diameter orifice. An auto-tune procedure has been performed in order to adjust the different internal parameters of the mass spectrometer and to optimize the signal intensity. A power of 200 W and a pressure of 1 Pa were used during this experiment.

2.3. Morphological and structural characterizations of films

The surface and cross-sectional morphology of the deposited films were investigated by scanning electron microscopy (Carl Zeiss SMT, Supra-40, FEG-SEM). The accelerating voltage in the range of 3-4 kV has been used. The evolution of the crystalline structure of Al films with different He concentrations was characterized using a Bruker D8 Discover X-ray diffractometer in the Grazing incidence geometry (GIXRD). In addition, the crystallite size (D) was determined from diffractograms obtained in the Bragg-Brentano configuration. The diffractometer is equipped with a Cu Kα radiation ($\lambda = 0.154$ nm) source, where 2ϴ was varied from 35 to 90° with 0.02°/step.

2.4. Composition of films

The quantity of Al in the films was determined by means of RBS with 2 MeV alpha particles. Moreover, the amount of He in the films was investigated by PEBS using 2.4 MeV protons. The Ion beam analysis (IBA) experiments were carried out at Pelletron accelerator facility of CEMHTI laboratory (Orléans), a facility that is part of the EMIR&A French network of accelerators (http://emir.in2p3.fr). A 25 mm^2 Passivated Implanted Planar Silicon (PIPS) detector is located at 166° scattering angle and 90 mm distance. The experimental spectra were simulated using the SIMNRA software [23] and the differential cross-sections for spectra simulation were determined from the SigmaCalc Internet site [24]. The proportion of He incorporated inside the films was determined as the ratio of the areal atomic density of He atoms ($\mathrm{N_{He}^{PEBS}}$) to that of Al atoms $\left(\mathrm{N_{Al}^{RBS}}\right)$. The uncertainty on $\mathrm{N_{Al}}$ was evaluated to ± 5% considering the statistical error on the Al RBS signal. Then, the uncertainty on He proportion was estimated to ± 15% taking into account the statistical error on both He PEBS and Al RBS signals.

3. Results

3.1. Plasma and sputtering process

Figure 1 shows the variation of the cathode voltage (V) as a function of the percentage of He in the gas phase. Three main zones could be identified. For zone A ($\Gamma_{\mathrm{He}} < 70\%$), the voltage remains approximately constant near 370 V. So, in this region, introducing He does not significantly modify the plasma. This is not surprising since He has a smaller ionization cross section ($\sigma_{\mathrm{He}} = 4.25 \times 10^{-21}$ m^2) than that of Ar ($\sigma_{\mathrm{Ar}} = 3.25 \times 10^{-20}$ m^2) [25].

In zone B, the absolute value of the voltage decreases from 370 to 320 V as the percentage of He increases from 70 to 93%, indicating that He starts influencing the plasma features. The observed trend at a fixed current suggests a rise of the ion flux at the cathode, revealing an increase in the electron and ion density. Several authors have studied the change in plasma characteristics when another inert gas is added to Ar in sputtering plasma discharges [26,27]. The primary reported changes were attributed to the difference of the ionization potential. It is known that the ionization energy of the gas atom plays a major role in different mechanisms that influence the ionization degree in the plasma [28]. Indeed, this parameter determines the secondary electron emission coefficient of the ions impacting the target [29], the electron impact ionization cross section of the gas atoms, and indirectly the electron energy distribution function. For instance, it has been shown that substituting argon (15.75 eV) by gases of higher ionization energies, like He (24.59 eV) [25] or Ne (21.6 eV) [30], induces an increase of the electronic temperature and thus the high energy electron contribution in the energy distribution function [31]. This leads to a rise in the ionization degree of other species (Ar and sputtered Al atoms) in the plasma. A high ionization potential promotes the secondary electron emission from the target which sustains the discharge and increases the electron and ion density. Moreover, in the particular case of Ar/He mixture, other mechanisms like asymmetric charge transfer and metastable-neutral ionization have been found to increase the ionization degree [32]. These observations are in agreement with the decrease in the cathode voltage absolute value observed in zone B.

In zone C, the voltage increases sharply, reaching 440 V for 100% He. This is the result of a transition from Ar to He-dominated plasma. At this step, the main partner of electron/neutral collisions becomes He, which leads to a less efficient ionization process and, thus, to a rapid decrease of the electron density. Again, to maintain the current constant, the cathode voltage has to increase in absolute value. Similar high values of the cathode voltage in absolute value have been reported in pure He or Ne sputtering discharges by several authors [26,33]. It was also reported that pure helium discharges were challenging to initiate due to the low ionization cross-section of He [25,33]. Therefore, ignition was maintained by increasing the pressure, pulsing the target power, or adding a small percentage of Ar gas. The sharp rise of the cathode voltage shown in Figure 1 indicates that the plasma regime is completely modified above 93 % of He in the gas phase, which is expected to influence the sputtering process and the film growth to a great extent.

The deposition rate of Al (ν_{Al}) has been determined from RBS measurements, which is the number of Al atoms deposited per unit of area and time. Figure 2 presents the variation of ν_{Al} as a function of the Γ_{He} in the gas phase. First, it is observed that the deposition rate remains high and approximately constant until 93% of He. Then, beyond 93%, the deposition rate decreases because He ions start contributing significantly to the sputtering of Al.

3.2. Energy distribution functions (EDF)

Figure 3 shows the energy distribution functions at the substrate position of Al atoms sputtered from the target by pure Ar^+ or He^+ ions. It is clearly shown that in pure He plasma, Al atoms will arrive at the substrate with a higher mean kinetic energy (2.7 eV compared to 0.16 eV in pure Ar). These results were expected and well known. For instance, Schuan et al. used a mixture of He and Ar to promote the energy of the depositing atoms and enhance Nb film quality [32]. The higher energy of Al atoms in case of He plasma could be explained by the low mass of He which reduces the energy loss by He atoms colliding with the sputtered gas atoms [32]. One has to keep in mind that besides these trends of the energy distribution function, shifting from Ar^+ to He^+ also reduces the number of sputtered Al atoms.

Another significant result is obtained from SRIM simulations showing that a non-negligible part of high energy He^+ ions (17%) is backscattered at the target. These ions become fast neutrals that interact with the substrate during the film growth. Considering the respective angular distributions of sputtered Al atoms and backscattered He^+ ions, a rough estimation yields that one fast He neutral arrives at the substrate for ten depositing Al atoms. Since the He^+ ions have been accelerated through the cathode sheath (400-440 eV), they exhibit a relatively high mean kinetic energy: 145 eV at the target and 60 eV 12 cm away at the substrate position, which is above the sputtering threshold of aluminum under He ion bombardment [34]. On the contrary, SRIM simulations predicted that the probability of Ar ions to be backscattered is negligible (less than 0.2%) in our experimental conditions.

Figure 4 displays the IEDF of Al^+, Ar^+ and He^+ ions between 1 and 20 eV obtained from the different gas mixtures. The ion energy distribution functions of Al^+ ions in different Ar/He gas mixtures exhibits an intense peak at low energy (below 1 eV) corresponding to the almost thermalized ionized sputtered species. This intense signal was not registered during the energy-resolved mass spectrometer measurements. Figure 4a shows the presence of energetic ionized population of sputtered aluminum usually observed for metals in DC magnetron discharges [27,35,36]. As Γ_{He} increases above 70%, the high energy tail is promoted showing that sputtered Al atoms lose less energy by collision during their transport towards the substrate. This is in good agreement with SRIM data obtained in pure Ar and He gas. Significant changes are observed in the energy distribution function of Ar^+ and He^+ at high Γ_{He}: the peak below 5 eV splits into two contributions and the high energy tail (between 5 eV and 10 eV) is enhanced. These trends are promoted as the He percentage increases in the gas phase. A complete understanding of the features of these energy distribution functions is beyond the scope of this paper. However, the impact of He metastable atoms present at high He partial pressure may be suspected. Nevertheless, regarding Al thin film growth, what has to be retained is the increase of the energy brought by the particles (sputtered Al, Ar^+, He^+, fast neutrals and metastable atoms) interacting with the substrate.

3.3. Thin film characteristics

Figure 5 presents cross-section and top-view SEM images of selected Al films obtained with different Γ_{He} in the gas phase. It is evident that the composition of the gas phase significantly influences film morphology. Films deposited with Γ_{He} lower than 70% are composed of large

3D faceted grains, as shown in Figure 5 (1,b) and Figure 5 (2,b). Even if a zone at the interface with the substrate seems to exhibit small pores, a very dense structure is observed over 2/3 of the thickness. The size of the grains is in the order of 200-300 nm. In the so-called structure zone model, this kind of morphology is usually observed in zone T, when the surface mobility of the depositing atoms is sufficient to induce initial grain coarsening [37–39]. As Γ_{He} increases up to about 90%, the grain size observed in top-view image decreases down to less than 100 nm. A quite dense columnar microstructure is visible on the cross-section images even if small voids exist between columns, as shown in Figure 5 (3,a). This columnar structure is typically obtained in the case of magnetron sputtered films deposited under limited mobility of adatoms such that the film growth is driven by surface shadowing [37]. The morphology of the 95% sample appears quite different from the previous ones. Clearly, two families of grains are visible, exhibiting different diameters and heights and surrounded by immense voids. The surface roughness is expected to be high, and the typical grain size ranges from 100 to 200 nm and 200 to 400 nm, as shown in Figure 5 (4,c). 50 nm pores are also present and distributed homogeneously along with the film thickness (Figure 5 (4,b)). Thereafter, a different morphology is obtained with pure He plasma. In this case, the film is completely porous, and it is composed of fiberform nanostructures (~ 100 nm in diameter) that seem to be grown perpendicular to the substrate surface and nanoparticles (10-20 nm in diameter), as shown in Figure 5 (5,a,b). The presence of these two microstructures in this film could result from two different Al deposition processes that will be discussed later.

The proportion of He to Al in the films, determined by RBS and PEBS measurements is shown in Figure 6. Helium is not detected in the films synthesized in He/Ar mixtures containing less than 20% of He. Moreover, He proportion remains very low (less than 5%) until 70% of He is added in the gas phase. Then, the proportion of He starts to increase, reaching a maximum of ~ 15% for the film deposited with 95% of He in the gas phase. The film deposited in pure He plasma, presenting the most porous sample, contains a limited amount of He (below 4%). All these trends suggest that different mechanisms of He trapping or desorption are involved depending on the plasma/deposition regime.

The influence of He concentration on the structural properties of Al films deposited with different Γ_{He} was also investigated by GIXRD. As shown in Figure 7a, all Al films exhibit the face-centered-cubic (fcc) crystal structure. The peaks corresponding to (111), (200), (220), (311), and (222) crystallographic planes are identified. The intensity of the peaks are similar to those given in the ICCD file (PDF card -00-004-0787) implying that Al films are polycrystalline and randomly oriented. Figure 7b presents a zoom on the angular 2θ domain restricted around the peak corresponding to the (111) plane for selected films. The intensity of this peak decreases as Γ_{He} increases, indicating that the proportion of the diffracting material becomes lower. Two interpretations may explain such result. First, the film is less crystallized under He incorporation. Second, the film becomes effectively more porous. Also, it can be clearly noticed that the peak broadens and shifts to lower angle values when the percentage of He in the gas phase increases from 9 to about 70%. After that, from 91 to 100% He, different evolution is observed: the peak shifts back to its initial value, whereas the width remains constant.

To get better insight into the peak width evolution, the crystallite size (D) of the different samples was determined from the width of the θ-2θ (111) peak, based on the Scherrer formula [40]. Despite the different deposition times, the thickness of the films was not the same. Since the crystallite size depends on film thickness [37], the crystallite size for an equivalent thickness of 1 µm was calculated. Figure 8 shows the evolution of this crystallite size. Again the same three zones can be identified on the graph. When Γ_{He} increases from 9 to 70%, the crystallite size of Al film decreases sharply from ~ 100 nm to ~ 30 nm. Between 70 and 93% He, the crystallite size is around 20 nm. Beyond 93%, a slight rise is visible, but the crystallite remains smaller than that in pure argon.

4. Discussion

The study of the deposition of Al films using different He/Ar gas mixtures allowed identifying three plasma regimes, as shown in Figure 1. The non-linear transition from Ar to He driven plasma has been found to modify the sputtering efficiency and the deposition conditions. Besides, the nature of the gas may impact the species ejected from the target and their energy distribution function at the substrate [26] (Figure 3). SRIM simulations predict the backscattering of a large number of high energy He^+ ions at the target that become fast neutrals and interact with the substrate during the film growth.

First, in zone A (Γ_{He} = 0-70%), the plasma is dominated by argon. Ar^+ ions are mainly present and induce the sputtering of the target atoms. Hence, the sputtering yield of Al is high, and the deposition rate remains high and constant in this range. The films show the dense columnar structure, as revealed by SEM images. Large and well crystallized Al grains are obtained. All these results indicate that the growth mode is not drastically modified in this range of He/Ar mixtures compared to pure Ar. Nevertheless, the size of the crystal domains decreases with increasing Γ_{He} (see Figure 8). Also, peak broadening from XRD analysis confirms a reduction in the crystallite size. Since the amount of He detected inside the film is very low and constant, this phenomenon could not be related to He trapping. Moreover, since Γ_{He} increases in the gas phase, the probability that a sputtered Al atom encounters collisions with a He atom rather than an Ar atom is promoted. Results obtained by SRIM show that this will lead to a rise in the mean kinetic energy carried by the depositing Al atoms. This trend is contradictory to the observed diminution of the crystallite size. However, another effect that could be invoked, when He is added in the gas phase, is the efficient cooling process due to the well-known high thermal conductivity of He [41]. The interaction of more He atoms with the substrate during the growth could reduce adatom mobility. Such a mechanism could also promote stress inside the film, which is in good agreement with the XRD peak shift observed (see Figure 7b).

In zone B (Γ_{He} = 70-95%), the addition of He in the gas mixture induces an increase of He atoms incorporated in the films by a factor of 3, affecting the growth. This is visible on the microstructure of the films that strongly varies in this domain (see Figure 5). From discharge parameters (Figure 1) and SRIM results, we can assume that helium ions begin to be formed and that more fast He neutrals and metastable atoms now reach the substrate. It has been previously proved that backscattered neutrals are responsible for the insertion of inert gas in magnetron sputtered thin films [42]. The increase of trapped He in the plasma regime where He ions are supposed to be formed agrees with this statement. The presence of pores on SEM images and the fact that the crystallite size does not vary in this zone reveal that He does not perturb the growth of Al grains but is instead trapped outside the Al lattice, forming bubbles at the grain boundaries. This is in agreement with what is widely known about He behavior in metals. Because He has no affinity with metals and diffuses easily, it tends to be retained in defects becoming efficient trapping sites, leading to the growth of He-vacancy complexes and then to bubbles [2,20].

Third, in zone C, especially in pure He, the growth regime is completely altered. This is clearly visible on the SEM images (Figure 5 (5,a,b,c)), where fiberform nanostructures coated by nanoparticles are obtained. To our knowledge, this kind of morphology is very unusual and has never been reported for Al thin films grown by magnetron sputtering. Since it has only been observed on the 100% He sample, it can be concluded that a significant change of the growth mode due to the modified plasma conditions and energy flux is certainly achieved in pure He plasma. Helium is no more efficiently inserted in the film or is desorbed during the growth, giving rise to the porous structure. A comparison with He implanted metal surfaces means that the release of the trapped He into bubbles enhances the formation of such fiber-like structure [43,44]. Tanyeli et al. published a comprehensive study on the surface modification of Ti, Cu, and Al after exposure to low energy He ions (< 100 eV) [14]. Different surface modifications were detected among these metals. Ti did not show significant surface modification, attributed to its closely packed structure and low sputtering yield [14]. However, in the case of Cu and Al, nanopillars have been obtained [14]. The authors explain that such patterns are formed when sputtering the surface and/or emptying of superficial bubbles are associated with a high atom mobility. Al is a perfect candidate for creating the fuzz structure due to its high sputtering yield by He^+ ions and low fusion temperature, ensuring high adatom mobility [14]. In our work, this fiber-like nanostructure is formed when favorable deposition conditions are met, which means when the ratio of fast He neutrals to the depositing Al atoms and when the energy transferred by all the particle impacting the substrate (sputtered Al, metastable He atoms, Ar^+ and He^+) are high. Then, the surface diffusion of deposited Al atoms is promoted.

As mentioned above, in pure He plasma, nanoparticles are also detected in the films. It is known that nanoparticles can be formed in the gas phase in magnetron sputtering, especially at high pressure, when collisions are enhanced [22,45]. This trend is well known and used in gas aggregation source devices [46–49]. He gas is usually employed in such experiments, again because of its cooling properties, to promote the condensation process [43]. We think that for high percentages of He in the gas phase, nucleation and growth of nanoparticles could occur in our experimental conditions.

5. Conclusions

In this study, we investigated the influence of He introduction in the gas phase during magnetron sputtering deposition of aluminum thin films to synthesize porous nanostructures. The addition of He in an Ar plasma affects the sputtering efficiency of the target, the transport of ejected metal atoms, the kinetics of the ionized species and the deposition conditions at the substrate. In a first wide range of Γ_{He} (below 70%), we found out that a cooling process by He gas could explain the decrease of the Al crystallite size, which is the main detected modification of Al film properties. A residual amount of He is inserted inside the films (trapped gas) that does not seem to affect the growth. Then, when He starts to be ionized in the plasma, the concentration of He atoms inserted in the film increases. It is mainly located in nanoscale bubbles, such that its presence significantly modifies the microstructure. This behavior is not far from what is observed during He ion implantation inside metals and is thus attributed to backscattered He neutrals interaction with the growing Al film. At very high Γ_{He} in the gas phase (above 95%), the role of these He fast neutrals is promoted since their number increases and the deposition rate decreases. Implantation leading to large bubble formation and emptying, as well as sputtering processes, can occur. At the same time, since the kinetic energy brought by Al depositing atoms rises, surface mobility is enhanced. These joint mechanisms lead to the formation of a fiberform or fuzz-like porous nanostructure. The presence of nanoparticles, not seen in He implantation experiments, could be explained by another Al deposition process: growth of nanoparticles in the gas phase that are deposited on the substrate. Complementary analyses of both the gas phase and the films are scheduled to deeper understand the growth processes in the three regimes evidenced in this first work. Regarding the application, films obtained in pure He gas will be tested for the hydrothermal synthesis of H_2.

CRediT authorship contribution statement

Sara: Conceptualization, Methodology, Writing, Review & editing. Fatima Zahrae: Formal analysis. Pascal: Methodology, Software and editing. Agnès: Formal analysis. Amaël: Investigation, Formal analysis and editing. Eric: Investigation, Formal analysis and editing. Thierry: Investigation, Formal analysis and editing. Asunción: Investigation, editing and Funding acquisition. Anne-Lise: Conceptualization, Supervision, Writing, Review & editing and Funding acquisition.

Declaration of competing interest

The authors declare that they have no known competing financial interests or personal relationships that could have appeared to influence the work reported in this paper.

Acknowledgements

This work was supported by the region of « Centre Val de Loire » and the European Regional Development Funds (FEDER). The authors thank LE STUDIUM Loire Valley Institute for Advanced studies, and Asunción Fernández thanks also the support by the Spanish grant no. RTI2018-093871-BI00 (co-financed by EU FEDER).

References

[1] H. Zheng, S. Liu, H. Yu, L. Wang, C. Liu, L. Shi, Introduction of helium into metals by magnetron sputtering deposition method, Mater. Lett. 59 (2005) 1071–1075.

[2] L. Shi, C. Liu, S. Xu, Z.Y. Zhou, Helium-charged titanium films deposited by direct current magnetron sputtering, Thin Solid Films. 479 (2005) 52–58.

[3] F. Chamssedine, T. Sauvage, S. Peuget, DIADDHEM set-up: New IBA facility for studying the helium behavior in nuclear glasses, Nucl. Instrum. Methods Phys. Res. Sect. B Beam Interact. Mater. At. 268 (2010) 1862–1866.

[4] L. Pentecoste, P. Brault, A.-L. Thomann, P. Desgardin, T. Lecas, T. Belhabib, M.-F. Barthe, T. Sauvage, Low Energy and low fluence helium implantations in tungsten: Molecular dynamics simulations and experiments, J. Nucl. Mater. 470 (2016) 44–54.

[5] L. Pentecoste, A.-L. Thomann, P. Brault, T. Lecas, P. Desgardin, T. Sauvage, M.-F. Barthe, Substrate temperature and ion kinetic energy effects on first steps of He^+ implantation in tungsten: Experiments and simulations, Acta Mater. 141 (2017) 47–58.

[6] I. Tanyeli, L. Marot, M.C. van de Sanden, G. De Temmerman, Nanostructuring of iron surfaces by low-energy helium ions, ACS Appl. Mater. Interfaces. 6 (2014) 3462–3468.

[7] L. Wang, T. Hao, B.-L. Zhao, T. Zhang, Q.-F. Fang, C.-S. Liu, X.-P. Wang, L. Cao, Evolution behavior of helium bubbles and thermal desorption study in helium-charged tungsten film, J. Nucl. Mater. 508 (2018) 107–115.

[8] H. Fan, Z. Wu, T. Sun, M. Yang, J. Guo, K. Yang, Y. Li, Efficient plasma-assisted approach in nanostructure fabrication of tungsten, Mater. Des. 89 (2016) 78–84. https://doi.org/10.1016/j.matdes.2015.09.139.

[9] S. Iyyakkunnel, L. Marot, B. Eren, R. Steiner, L. Moser, D. Mathys, M. Düggelin, P. Chapon, E. Meyer, Morphological changes of tungsten surfaces by low-flux helium plasma treatment and helium incorporation via magnetron sputtering, ACS Appl. Mater. Interfaces. 6 (2014) 11609–11616.

[10] S. Takamura, N. Ohno, D. Nishijima, S. Kajita, Formation of nanostructured tungsten with arborescent shape due to helium plasma irradiation, Plasma Fusion Res. 1 (2006) 051–051.

[11] S. Kajita, T. Saeki, Y. Hirahata, M. Yajima, N. Ohno, R. Yoshihara, N. Yoshida, Development of nanostructured black metal by self-growing helium bubbles for optical application, Jpn. J. Appl. Phys. 50 (2011) 08JG01.

[12] S. Kajita, T. Yoshida, D. Kitaoka, R. Etoh, M. Yajima, N. Ohno, H. Yoshida, N. Yoshida, Y. Terao, Helium plasma implantation on metals: Nanostructure formation and visible-light photocatalytic response, J. Appl. Phys. 113 (2013) 134301.

[13] F. Giarratano, G. Arzac, V. Godinho, D. Hufschmidt, M.J. De Haro, O. Montes, A. Fernández, Nanoporous Pt-based catalysts prepared by chemical dealloying of magnetron-sputtered Pt-Cu thin films for the catalytic combustion of hydrogen, Appl. Catal. B Environ. 235 (2018) 168–176.

[14] I. Tanyeli, L. Marot, D. Mathys, M.C. Van De Sanden, G. De Temmerman, Surface modifications induced by high fluxes of low energy helium ions, Sci. Rep. 5 (2015) 1–9.

[15] V. Godinho, P. Moskovkin, R. Álvarez, J. Caballero-Hernández, R. Schierholz, B. Bera, J. Demarche, A. Palmero, A. Fernández, S. Lucas, On the formation of the porous structure in nanostructured a-Si coatings deposited by dc magnetron sputtering at oblique angles, Nanotechnology. 25 (2014) 355705.

[16] B. Lacroix, V. Godinho, A. Fernández, The nanostructure of porous cobalt coatings deposited by magnetron sputtering in helium atmosphere, Micron. 108 (2018) 49–54.

[17] R. Schierholz, B. Lacroix, V. Godinho, J. Caballero-Hernández, M. Duchamp, A. Fernández, STEM–EELS analysis reveals stable high-density He in nanopores of amorphous silicon coatings deposited by magnetron sputtering, Nanotechnology. 26 (2015) 075703.

[18] A. Fernández, D. Hufschmidt, J.L. Colaux, J.J. Valiente-Dobón, V. Godinho, M.C.J. de Haro, D. Feria, A. Gadea, S. Lucas, Low gas consumption fabrication of 3He solid targets for nuclear reactions, Mater. Des. 186 (2020) 108337.

[19] J.M. Bergthorson, Recyclable metal fuels for clean and compact zero-carbon power, Prog. Energy Combust. Sci. 68 (2018) 169–196. https://doi.org/10.1016/j.pecs.2018.05.001.

[20] C.-Z. Liu, L. Shi, Z. Zhou, X. Hao, B. Wang, S. Liu, L. Wang, Investigations of helium incorporated into a film deposited by magnetron sputtering, J. Phys. Appl. Phys. 40 (2007) 2150.

[21] J.F. Ziegler, M.D. Ziegler, J.P. Biersack, SRIM–The stopping and range of ions in matter (2010), Nucl. Instrum. Methods Phys. Res. Sect. B Beam Interact. Mater. At. 268 (2010) 1818–1823.

[22] L. Xie, P. Brault, J.-M. Bauchire, A.-L. Thomann, L. Bedra, Molecular dynamics simulations of clusters and thin film growth in the context of plasma sputtering deposition, J. Phys. Appl. Phys. 47 (2014) 224004.

[23] M. Mayer, Improved physics in SIMNRA 7, 21st Int. Conf. Ion Beam Anal. 332 (2014) 176–180. https://doi.org/10.1016/j.nimb.2014.02.056.

[24] A. Gurbich, SigmaCalc recent development and present status of the evaluated cross-sections for IBA, Nucl. Instrum. Methods Phys. Res. Sect. B Beam Interact. Mater. At. 371 (2016) 27–32.

[25] M.E. Abdel-kader, W.H. Gaber, F.A. Ebrahim, M.A. Abd Al-Halim, Characterization of the electrical breakdown for DC discharge in Ar-He gas mixture, Vacuum. 169 (2019) 108922. https://doi.org/10.1016/j.vacuum.2019.108922.

[26] G. West, P. Kelly, Influence of inert gas species on the growth of silver and molybdenum films via a magnetron discharge, Surf. Coat. Technol. 206 (2011) 1648–1652.

[27] A. Aijaz, K. Sarakinos, D. Lundin, N. Brenning, U. Helmersson, A strategy for increased carbon ionization in magnetron sputtering discharges, Diam. Relat. Mater. 23 (2012) 1–4.

[28] S. Cuynet, T. Lecas, A. Caillard, P. Brault, An efficient way to evidence and to measure the metal ions fraction in high power impulse magnetron sputtering (HiPIMS) post-discharge with Pt, Au, Pd and mixed targets, J. Plasma Phys. 82 (2016) 695820601.

[29] J.T. Gudmundsson, D. Lundin, N. Brenning, M.A. Raadu, C. Huo, T.M. Minea, An ionization region model of the reactive Ar/O2 high power impulse magnetron sputtering discharge, Plasma Sources Sci. Technol. 25 (2016) 065004.

[30] R.H. Livengood, S. Tan, R. Hallstein, J. Notte, S. McVey, F.F. Rahman, The neon gas field ion source—a first characterization of neon nanomachining properties, Nucl. Instrum. Methods Phys. Res. Sect. Accel. Spectrometers Detect. Assoc. Equip. 645 (2011) 136–140.

[31] B.B. Sahu, S.I. Kim, M.W. Lee, J.G. Han, Effect of helium incorporation on plasma parameters and characteristic properties of hydrogen free carbon films deposited using DC magnetron sputtering, J. Appl. Phys. 127 (2020) 014901.

[32] G. Schucan, S. Calatroni, C. Benvenuti, Niobium films produced by magnetron sputtering using an Ar-He mixture as discharge gas, Proc. 7th Int. Conf. RF Superconductivity (SRF'95) (1995) 479-483. paper ID: SRF95C22.

[33] Y. Kusano, Z.H. Barber, J.E. Evetts, I.M. Hutchings, Influence of inert gases on ionized magnetron plasma deposition of carbon nitride thin films, Proc. Eight Int. Conf. Plasma Surf. Eng. 174–175 (2003) 601–605. https://doi.org/10.1016/S0257-8972(03)00326-8.

[34] Y. Yamamura, H. Tawara, Energy dependence of ion-induced sputtering yields from monatomic solids at normal incidence, At. Data Nucl. Data Tables. 62 (1996) 149–253.

[35] J.M. Andersson, E. Wallin, E. Münger, U. Helmersson, Energy distributions of positive and negative ions during magnetron sputtering of an Al target in Ar/O_2 mixtures, J. Appl. Phys. 100 (2006) 033305.

[36] J.T. Gudmundsson, Physics and technology of magnetron sputtering discharges, Plasma Sources Sci. Technol. 29 (2020) 113001.

[37] I. Petrov, P. Barna, L. Hultman, J. Greene, Microstructural evolution during film growth, J. Vac. Sci. Technol. Vac. Surf. Films. 21 (2003) S117–S128.

[38] S. Mahieu, P. Ghekiere, D. Depla, R. De Gryse, Biaxial alignment in sputter deposited thin films, Thin Solid Films. 515 (2006) 1229–1249.

[39] A. Anders, A structure zone diagram including plasma-based deposition and ion etching, Thin Solid Films. 518 (2010) 4087–4090.

[40] A.L. Patterson, The Scherrer Formula for X-Ray Particle Size Determination, Phys. Rev. 56 (1939) 978–982. https://doi.org/10.1103/PhysRev.56.978.

[41] A. B. Murphy, Transport coefficients of helium and argon-helium plasmas, IEEE Trans. Plasma Sci. 25 (1997) 809–814. https://doi.org/10.1109/27.649574.

[42] D. Hoffman, J.A. Thornton, Compressive stress and inert gas in Mo films sputtered from a cylindrical-post magnetron with Ne, Ar, Kr, and Xe, J. Vac. Sci. Technol. 17 (1980) 380–383.

[43] Y. Kikuchi, T. Okumura, K. Kadowaki, T. Aota, S. Maenaka, K. Fujita, S. Takamura, Porous tungsten nanostructure formation using a helium arc discharge plasma under sub-atmospheric pressure, J. Phys. Appl. Phys. 52 (2019) 375201. https://doi.org/10.1088/1361-6463/ab2ac1.

[44] X. Liu, Y.Y. Lian, H. Greuner, B. Boeswirth, Y.Z. Jin, F. Feng, J.B. Wang, L. Chen, J.P. Song, Y. Yu, T. Zhang, C.S. Liu, J. Tan, D.P. Liu, X.R. Duan, Irradiation effects of hydrogen and helium plasma on different grade tungsten materials, Proc. 22nd Int. Conf. Plasma Surf. Interact. 2016 22nd PSI. 12 (2017) 1314–1318. https://doi.org/10.1016/j.nme.2017.01.018.

[45] T. Peter, M. Wegner, V. Zaporojtchenko, T. Strunskus, S. Bornholdt, H. Kersten, F. Faupel, Metal/polymer nanocomposite thin films prepared by plasma polymerization and high pressure magnetron sputtering, PSE 2010 Spec. Issue. 205 (2011) S38–S41. https://doi.org/10.1016/j.surfcoat.2010.12.045.

[46] C. Binns, Nanoclusters deposited on surfaces, Surf. Sci. Rep. 44 (2001) 1–49.

[47] M. Ganeva, T. Peter, S. Bornholdt, H. Kersten, T. Strunskus, V. Zaporojtchenko, F. Faupel, R. Hippler, Mass Spectrometric Investigations of Nano-Size Cluster Ions Produced by High Pressure Magnetron Sputtering, Contrib. Plasma Phys. 52 (2012) 881–889.

[48] A. Caillard, S. Cuynet, T. Lecas, P. Andreazza, M. Mikikian, A.-L. Thomann, P. Brault, PdPt catalyst synthesized using a gas aggregation source and magnetron sputtering for fuel cell electrodes, J. Phys. Appl. Phys. 48 (2015) 475302. https://doi.org/10.1088/0022-3727/48/47/475302.

[49] P. Brault, W. Chamorro-Coral, S. Chuon, A. Caillard, J.-M. Bauchire, S. Baranton, C. Coutanceau, E. Neyts, Molecular dynamics simulations of initial Pd and PdO nanocluster growth in a magnetron gas aggregation source, Front. Chem. Sci. Eng. 13 (2019) 324–329.

Table 1: Deposition conditions of Al films in various He/Ar mixtures.

Γ_{He} (%)	Φ_{Ar} (sccm)	Φ_{He} (sccm)	t_d (min)	V (V)
0	20	0	30	370
9	20	2	30	370
33	20	10	30	367
50	20	20	30	363
67	5	10	45	361
71	4	10	45	360
77	3	10	45	358
91	1	10	45	330
93	1	14	45	320
95	1	20	45	325
100	0	10	60	439

Figure captions

Figure 1: Variation of the cathode voltage versus the percentage of He in the gas phase. Three sputtering regimes could be identified.

Figure 2: Al deposition rate for different He percentages (Γ_{He}).

Figure 3: Energy distribution functions of Al atoms at the substrate calculated by SRIM software (50000 launched Al atoms).

Figure 4: Experimental ion energy distribution function of (a) Al^+, (b) Ar^+ and (c) He^+ ions obtained from different gas mixtures (0, 50, 80, 90, 95 and 96% He).

Figure 5: (1,2,3 a) Cross-section and (1,2,3 b) top-view SEM images of Al films deposited with low Γ_{He}. (4,5, a) Cross-section SEM images and (4,5, b) images at higher magnification showing the presence of pores and nanostructures in the films deposited with high Γ_{He}. (4,5, c) Top-view SEM images of Al films deposited with high Γ_{He}.

Figure 6: Evolution of the proportion of He to Al in the films as a function of the percentage of He in the gas phase.

Figure 7: (a) GIXRD patterns of Al films and (b) zoom on the main peak (111) for films deposited with different He percentages. The vertical lines show the peak positions corresponding to Al (PDF card -00-004-0787).

Figure 8: Evolution of the crystallite size of the different samples for an equivalent thickness of 1 µm.

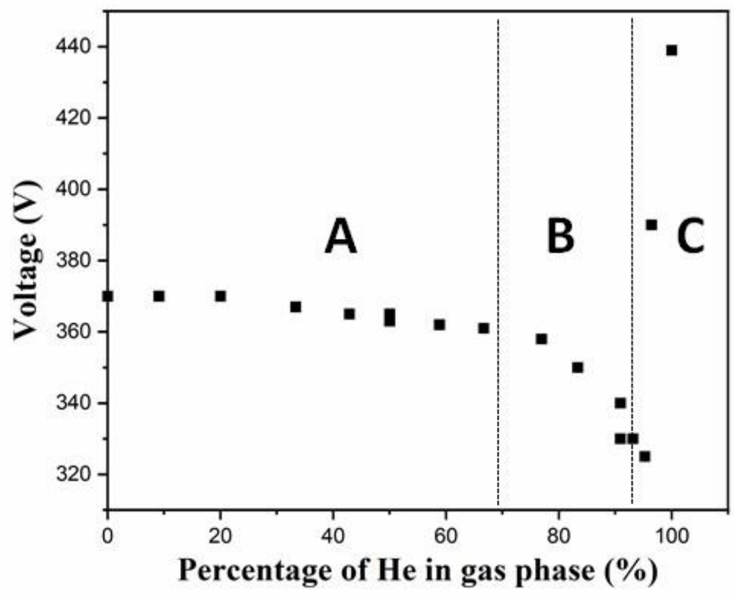

Figure 1

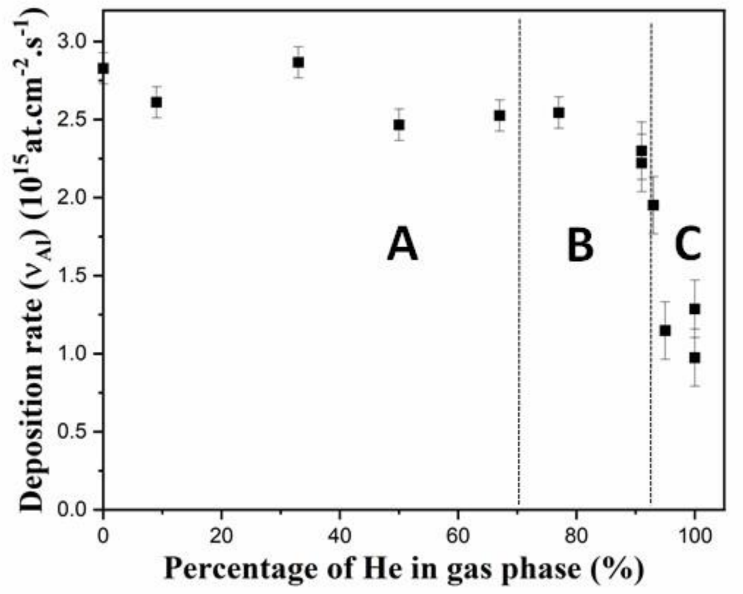

Figure 2

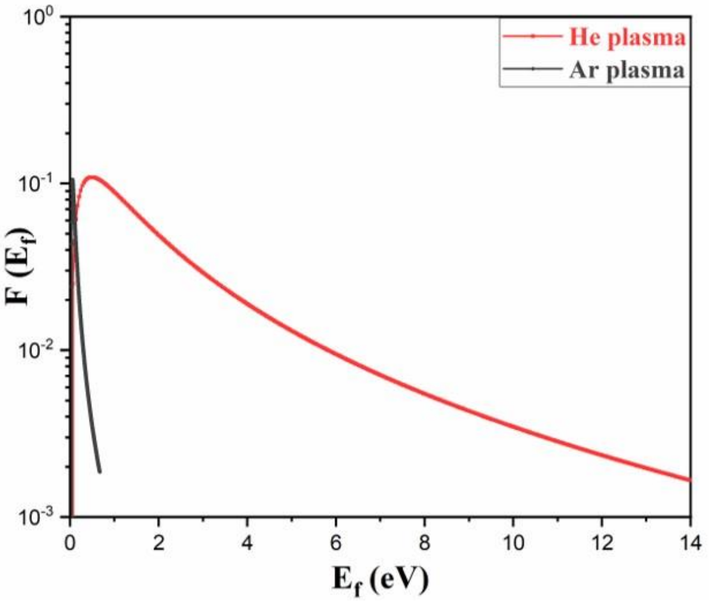

Figure 3

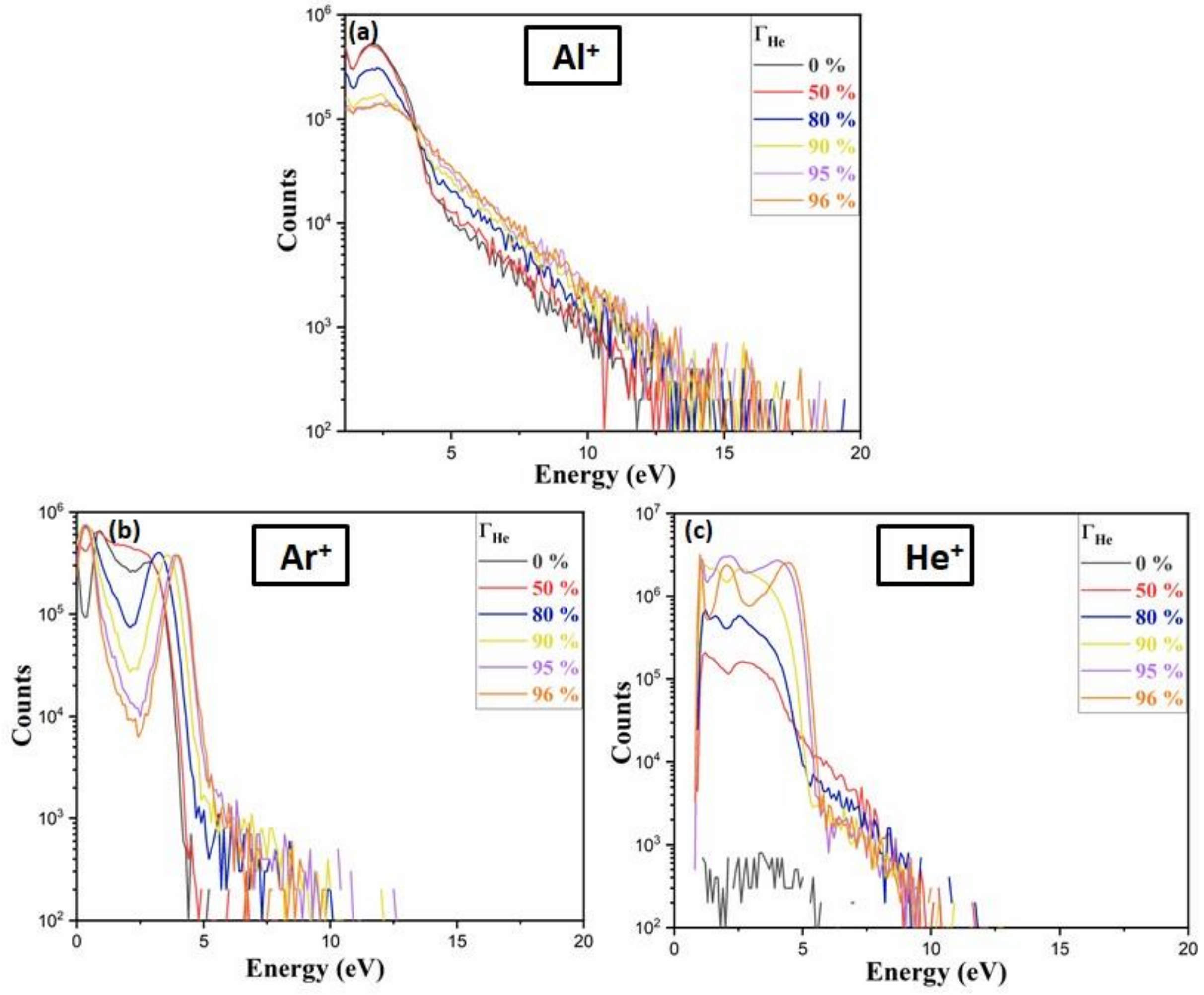

Figure 4

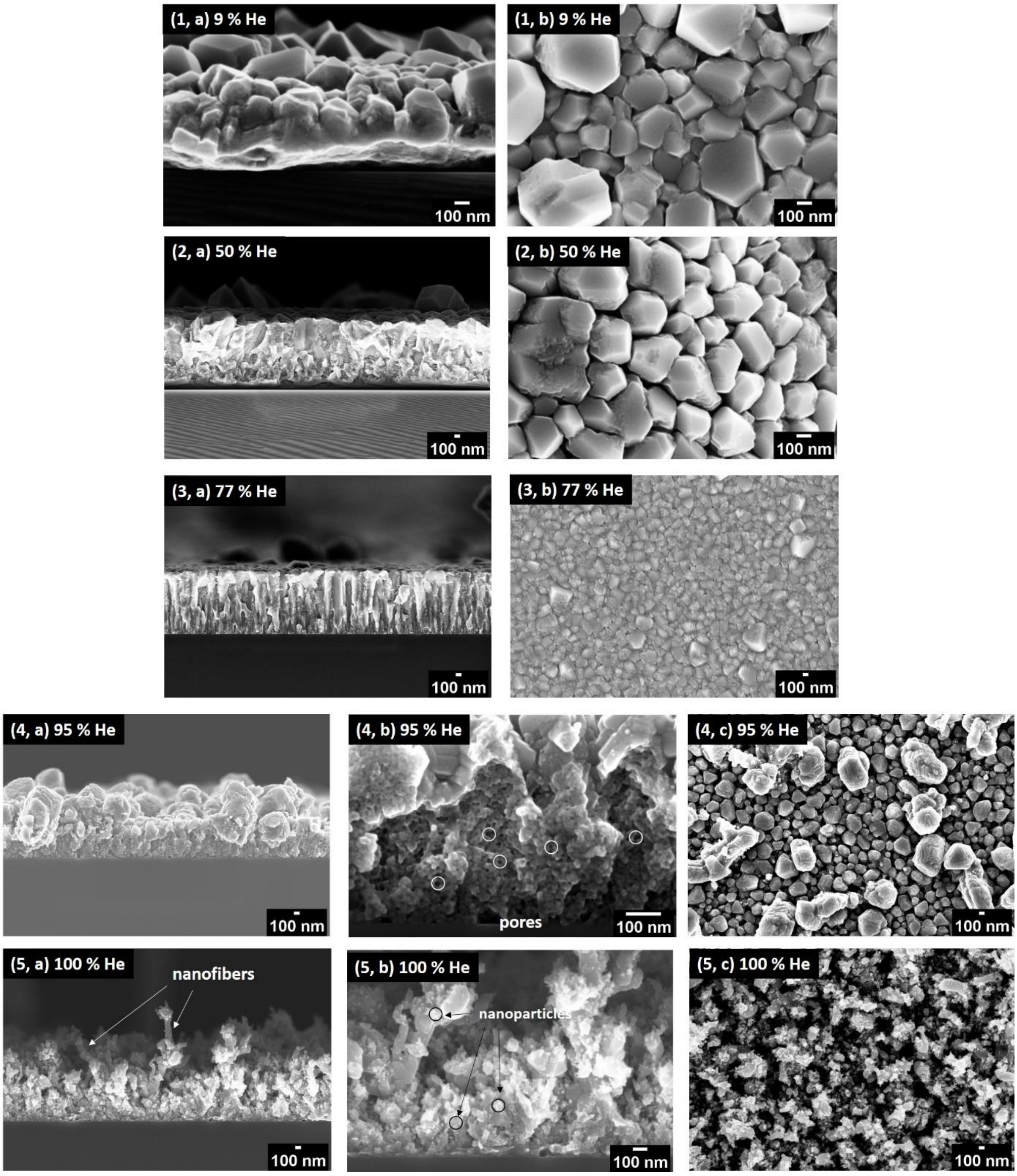
(1, a) 9 % He
100 nm
(1, b) 9 % He
100 nm
(2, a) 50 % He
100 nm
(2, b) 50 % He
100 nm
(3, a) 77 % He
100 nm
(3, b) 77 % He
100 nm
(4, a) 95 % He
100 nm
(4, b) 95 % He
pores
100 nm
(4, c) 95 % He
100 nm
(5, a) 100 % He
nanofibers
100 nm
(5, b) 100 % He
nanoparticles
100 nm
(5, c) 100 % He
100 nm

Figure 5

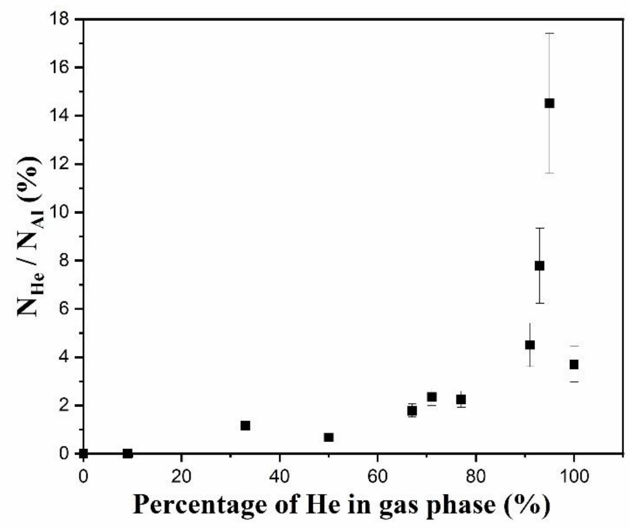

Figure 6

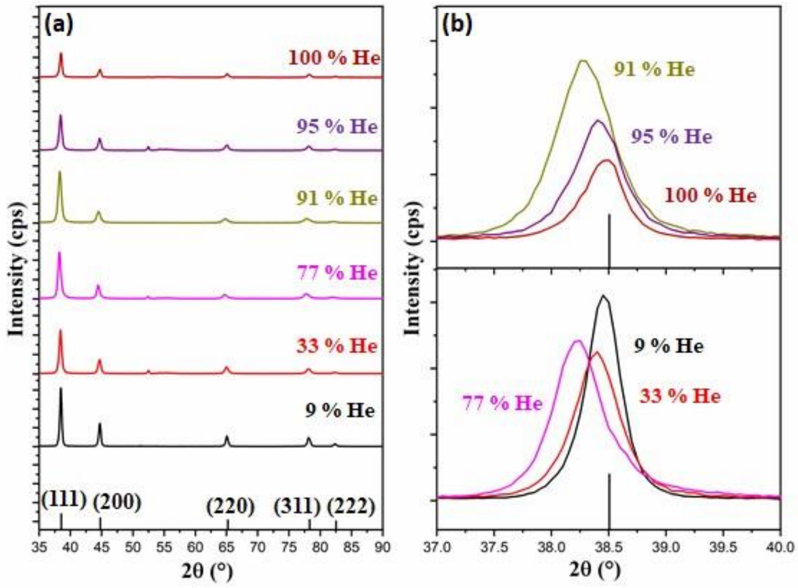

Figure 7

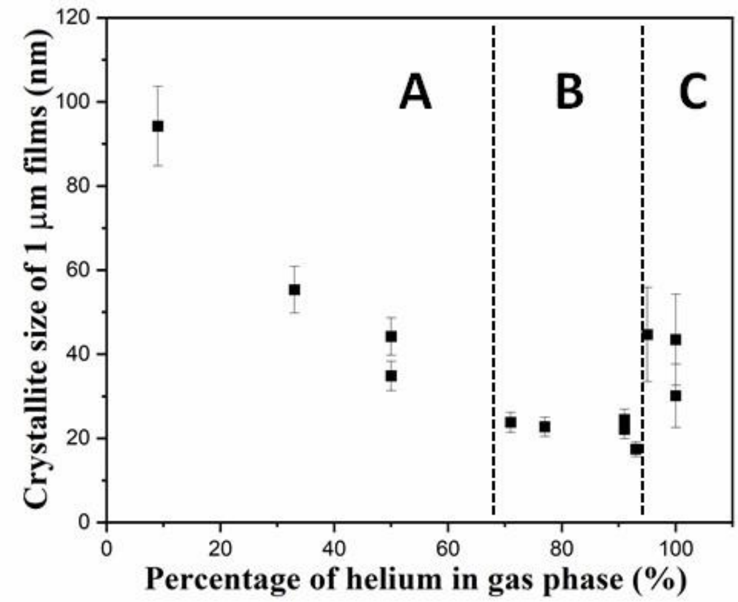
Crystallite size of 1 μm films (nm)
Percentage of helium in gas phase (%)
A
B
C
0
20
40
60
80
100
120
0
20
40
60
80
100

Figure 8